



Article

Structural Diversity of Mercury(II) Halide Complexes Containing Bis-pyridyl-bis-amide with Bulky and Angular Backbones: Ligand Effect and Metal Sensing

Manivannan Govindaraj ¹, Wei-Chun Huang ¹, Chia-Yi Lee ¹, Venkatesan Lakshmanan ¹, Yu-Hsiang Liu ¹, Pamela Berilyn So ², Chia-Her Lin ^{2,*} and Jhy-Der Chen ^{1,*}

¹ Department of Chemistry, Chung-Yuan Christian University, Chung Li, Taoyuan 320, Taiwan; manivannanjent@gmail.com (M.G.); learn122568@gmail.com (W.-C.H.); miss10031031@gmail.com (C.-Y.L.); flower95@gmail.com (V.L.); g10963021@cycu.edu.tw (Y.-H.L.)

² Department of Chemistry, National Taiwan Normal University, Taipei 106, Taiwan; pbtiuso@gmail.com

* Correspondence: chiaher@ntnu.edu.tw (C.-H.L.); jdchen@cycu.edu.tw (J.-D.C.); Tel.: +886-3-265-3351 (J.-D.C.)

Abstract: Hg(II) halide complexes [HgCl₂] 2L¹ [L¹ = *N,N'*-bis(3-pyridyl)bicyclo(2,2,2)oct-7-ene-2,3,5,6-tetracarboxylic diamide), **1**, [HgBr₂(L¹)_n], **2**, [HgI₂(L¹)], **3**, [Hg₂X₄(L²)₂] [X = Cl, **4**, Br, **5**, and I, **6**; L² = *N,N'*-bis(4-pyridylmethyl)bicyclo(2,2,2)oct-7-ene-2,3,5,6-tetracarboxylic diamide] and {[HgX₂(L³)]·H₂O}_n [X = Cl, **7**, Br, **8** and I, **9**; L³ = 4,4'-oxybis(*N*-(pyridine-3-yl)benzamide)] are reported and structurally characterized using single-crystal X-ray diffraction analyses. The linear HgCl₂ units of complex **1** are interlinked by the L¹ ligands through Hg---N and Hg---O interactions, resulting in 1D supramolecular chains. Complex **2** shows 1D zigzag chains interlinked through the Br---Br interactions to form 1D looped supramolecular chains, while the mononuclear [HgI₂L²] molecules of **3** are interlinked through Hg---O and I---I interactions, forming 2D supramolecular layers. Complexes **4**–**6** are isomorphous dinuclear metallocycles, and **7**–**9** form isomorphous 1D zigzag chains. The roles of the ligand type and the halide anion in determining the structural diversity of **1**–**9** is discussed and the luminescent properties of **7**–**9** evaluated. Complexes **7**–**9** manifest stability in aqueous environments. Moreover, complexes **7** and **8** show good sensing towards Fe³⁺ ions with low detection limits and good reusability up to five cycles, revealing that the Hg-X---Fe³⁺ (X = Cl and Br) interaction may have an important role in determining the quenching effect of **7** and **8**.

Keywords: Hg(II) complex; Hg(II) coordination polymer; crystal structure analysis; halide anion effect



Citation: Govindaraj, M.; Huang, W.-C.; Lee, C.-Y.; Lakshmanan, V.; Liu, Y.-H.; So, P.B.; Lin, C.-H.; Chen, J.-D. Structural Diversity of Mercury(II) Halide Complexes Containing Bis-pyridyl-bis-amide with Bulky and Angular Backbones: Ligand Effect and Metal Sensing. *Int. J. Mol. Sci.* **2022**, *23*, 7861. <https://doi.org/10.3390/ijms23147861>

Academic Editor: Zdeněk Trávníček

Received: 20 June 2022

Accepted: 15 July 2022

Published: 16 July 2022

Publisher's Note: MDPI stays neutral with regard to jurisdictional claims in published maps and institutional affiliations.



Copyright: © 2022 by the authors. Licensee MDPI, Basel, Switzerland. This article is an open access article distributed under the terms and conditions of the Creative Commons Attribution (CC BY) license (<https://creativecommons.org/licenses/by/4.0/>).

1. Introduction

The investigation of the rational design and synthesis of novel coordination polymers (CPs) continues to be an intense area of research due to their interesting structural diversity and potential industrial applications [1–3]. Although many remarkable CPs have been reported, it remains elusive to predict the structural types of the various CPs prepared. While choosing the appropriate metal cations and organic spacers is essential, the structural diversity of CPs is also subject to the identity of the counterions and the reaction conditions involved, such as the metal-to-ligand ratio, the solvent system, and the reaction temperature. In the same way, the halide anions have shown significant influence on the structures of the Hg(II) complexes, but it is difficult to predict which anions give similar or different structures [4–10]. In some cases, the chloride and bromide anions have no contribution on structural diversity, but the iodide anion has; while in other cases, the halide anions yield the same contribution to the structures [11–13]. For example, the reactions of HgX₂ (X = Cl, Br and I) with the ligand *N,N,N',N'*-tetrakispropyl-3,4-pyridinedicarboxamide afforded 2D CPs for the three anions, whereas those with *N,N,N',N'*-tetrakisobutyl-3,4-pyridinedicarboxamide gave 2D CPs for the chloride and bromide anions and a dimeric complex for the iodide anion [6]. On the other hand, the complexes formed by the reactions of HgX₂ with 2-pyridine piconyl hydrazone, 2-acetylpyridine

piconyl hydrazone, or 2-phenylpyridine piconyl hydrazone are all mononuclear, showing interesting weak interactions that differentiate these complexes [7]. However, using the bis-(3-pyridyl)isophthalamide ligand, bimetallic macrocycles for X = Cl and Br and 1D CP for X = I were produced, respectively [11]. The effect of the halide anion on the structural diversity of the formamidinate-based CPs has also been reported. While the 3D (X = Cl) and 2D (X = Br and I) heteronuclear CPs based on quadruple-bonded dimolybdenum units were obtained from the reactions of $[\text{Mo}_2(4\text{-pyf})_4]$ (4-Hpyf = 4-pyridylformamidine) with HgX_2 [12], the reactions of 4-Hpyf with HgX_2 afforded a 2D layer for X = Cl and 1D helical chains for X = Br and I, respectively [13].

Previously, we reported several bis-pyridyl-bis-amide (bpba)-based 1D Hg(II) halide CPs [14–17]. By using the rigid and isomeric 2,2-(1,2-phenylene)-bis(N-pyridin-3-yl)acetamide (1,2-pbpa), 2,2'-(1,3-phenylene)-bis(N-(pyridin-3-yl)acetamide (1,3-pbpa), and 2,2-(1,4-phenylene)-bis(N-(pyridin-3-yl)acetamide (1,4-pbpa), several CPs showing 1D zigzag, helical, mesohelical, and sinusoidal structures were prepared [14–16], while using the rigid *N,N'*-di(pyridin-3-yl)naphthalene-1,4-dicarboxamide (dpndc) afforded isostructural and helical CPs [17]. The structural diversity of these Hg(II) halide CPs containing rigid bpba are thus subject to the ligand types, whereas the role of the halide anions is only suggestive [14–17]. On the other hand, the pairs of supramolecular isomers with the flexible *N,N'*-di(3-pyridyl)adipoamide (L), $[\text{HgBr}_2(\text{GAG-L})]_n$ and $[\text{HgBr}_2(\text{AAA-L})]_n$ and $[\text{HgI}_2(\text{GAG-L})]_n$ and $[\text{HgI}_2(\text{AAA-L})]_n$, exhibit mesohelical, helical, sinusoidal, and helical chains, respectively [18].

Although there are already several organic ligand-supported Hg(II) halide complexes reported, research towards understanding the general effect of the halide anion on their structural diversity is less. Moreover, it is well known that the bpba ligands may easily be tailored to form structures with different flexibility and different shapes [14–18]; thus, in this report, we intend to investigate the effect of the halide anion on the structural types of the Hg(II) halide complexes containing bpba ligands with a bulky and angular backbone. We prepared two bpba ligands with bulky backbones, namely *N,N'*-bis(3-pyridyl)bicyclo(2,2,2)oct-7-ene-2,3,5,6-tetracarboxylic diamide (**L**¹), Figure 1a, and *N,N'*-bis(4-pyridylmethyl)bicyclo(2,2,2)oct-7-ene-2,3,5,6-tetracarboxylic diamide (**L**²), Figure 1b, as well as a bpba ligand with an angular backbone, namely 4,4'-oxybis(N-(pyridine-3-yl)benzamide) (**L**³), Figure 1c. Their corresponding reactions with Hg(II) halide salts were carried out. The synthesis and structures of $[\text{HgCl}_2] \cdot 2\text{L}^1$, **1**, $[\text{HgBr}_2\text{L}^1]_n$, **2**, $[\text{HgI}_2\text{L}^1]$, **3**, $[\text{Hg}_2\text{X}_4(\text{L}^2)_2]$ (X = Cl, **4**; Br, **5**; I, **6**), and $[\text{HgX}_2(\text{L}^3) \text{H}_2\text{O}]_n$ (X = Cl, **7**, Br, **8** and I, **9**) form the subject of this report, and the effect of the ligand type and halide anion on the structural diversity is discussed. The luminescence properties of **7** and **8** provide a unique opportunity to investigate the role of the halide anions in determining the sensing properties of the 1D bpba-based Hg(II) CPs.

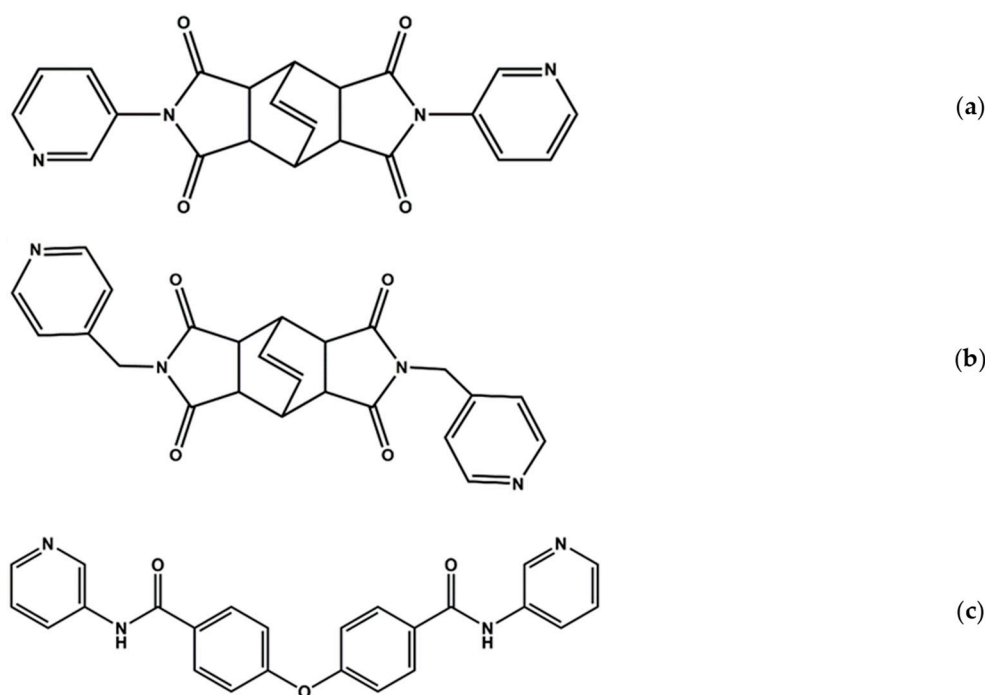


Figure 1. Structures of (a) L^1 , (b) L^2 , and (c) L^3 .

2. Results and Discussion

2.1. Crystal Structure of 1

Crystals of **1** conform to triclinic space group $P\bar{1}$ with a half Hg(II) ion, one chloride anion, and one L^1 ligand in the asymmetric unit. Figure 2a shows the coordination environment of the Hg(II) metal center, which is two-coordinated by two symmetry-related chloride anions [$\text{Hg}-\text{Cl} = \text{Hg}-\text{Cl}(\text{A}) = 2.3055(5) \text{ \AA}$], resulting in a linear geometry for the Hg(II) ion [$\angle \text{Cl}-\text{Hg}-\text{Cl}(\text{A}) = 180^\circ$]. Moreover, the linear metal units interact with the L^1 ligands in two directions, orthogonal to the linear metal unit through $\text{Hg}\cdots\text{N}$ [$\text{Hg}\cdots\text{N}(\text{1}) = \text{Hg}\cdots\text{N}(\text{1A}) = 2.727(1) \text{ \AA}$] and $\text{Hg}\cdots\text{O}$ [$\text{Hg}\cdots\text{O}(\text{3B}) = \text{Hg}\cdots\text{O}(\text{3C}) = 3.122(1) \text{ \AA}$] interactions, resulting in octahedral fashions for the Hg(II) ions, leading to the formation of a 1D linear supramolecular chain, Figure 2b. The sum of the van der Waals radius of Hg and N is 3.07 \AA , and that of Hg and O is 3.10 \AA (van der Waals radius: Hg = 1.55 , N = 1.52 , and O = 1.55 \AA).

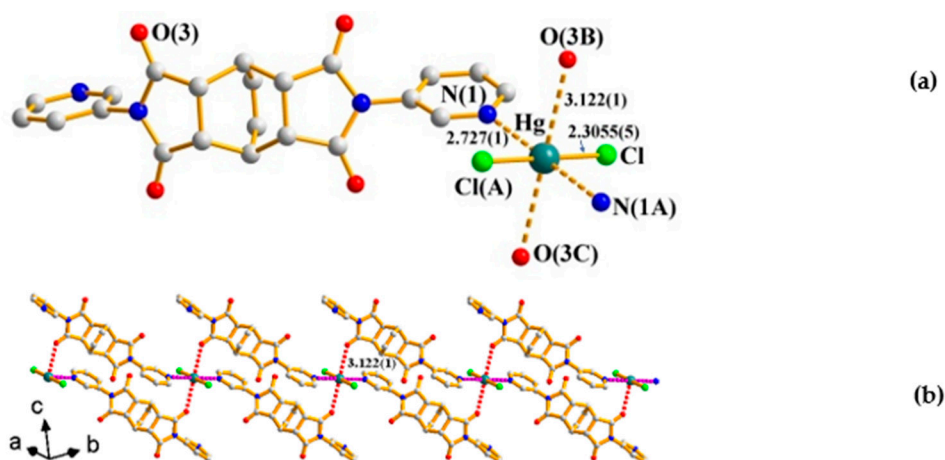


Figure 2. (a) Coordination environment of Hg(II) ion in **1**. Symmetry transformations used to generate equivalent atoms: (A) $-x, -y + 2, -z + 1$; (B) $-x + 1, -y + 1, -z + 1$; (C) $x - 1, y + 1, z$. (b) A depiction showing the 1D supramolecular structure of **1**.

2.2. Crystal Structure of 2

Crystals of **2** conform to triclinic space group $P\bar{1}$ with one Hg(II) ion, two bromide anions, and one L^1 ligand in each asymmetric unit. Figure 3a shows the coordination environment of the Hg(II) metal center, which is four-coordinated by two nitrogen atoms from two L^1 ligands [Hg-N(1) = 2.373(3); Hg-N(4A) = 2.435(3) Å] and two Br[−] anions [Hg-Br(1) = 2.4472(5); Hg-Br(2) = 2.5180(4) Å], resulting in a distorted tetrahedral geometry ($\tau_4 = 0.81$) for the Hg(II) ion, with bond angles of N(1)-Hg-N(4A) = 89.77(11), N(1)-Hg-Br(1) = 110.48(8), N(4A)-Hg-Br(1) = 104.32(8), N(1)-Hg-Br(2) = 102.94(7), N(4A)-Hg-Br(2) = 105.28(8) and Br(1)-Hg-Br(2) = 134.87(2). The Hg(II) cations are connected by the L^1 ligands to form 1D zigzag chains, which are further linked by the bromide anions through the Br \cdots Br interactions of 3.646(1) Å, that is significantly shorter than the sum of two van der Waals radii of Br (3.70 Å), resulting in 1D looped supramolecular chains, Figure 3b.

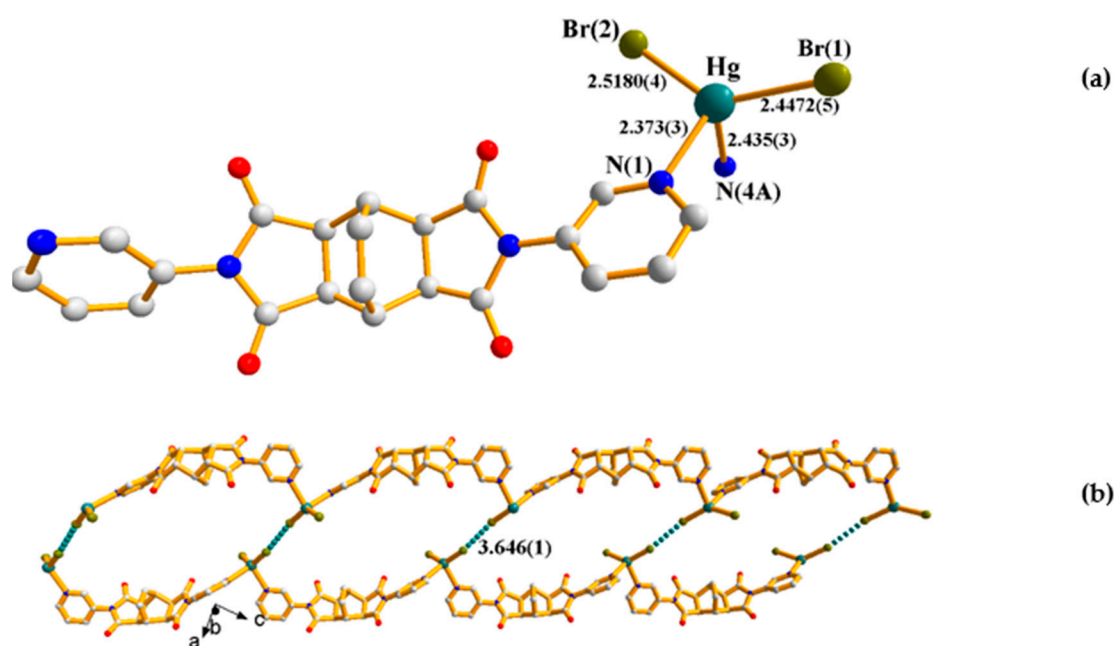


Figure 3. (a) Coordination environment about the Hg(II) ion in **2**. Symmetry transformations used to generate equivalent atoms: (A) $x - 1, y, z + 1$. (b) A drawing showing the 1D looped supramolecular chain.

2.3. Crystal Structure of 3

Crystals of **3** conform to triclinic space group $P\bar{1}$ with one Hg(II) ion, two iodide anions, and one L^1 ligand in each asymmetric unit. Figure 4a shows the coordination environment of the Hg(II) metal center of the mononuclear **3**, which is three-coordinated by one nitrogen atom [Hg-N(1) = 2.362(3) Å] and two iodide anions [Hg-I(1) = 2.6272(3) Å; Hg-I(2) = 2.6290(3) Å], resulting in a trigonal planar geometry for the Hg(II) ion [\angle I(1)-Hg-I(2) = 151.699(8) $^\circ$; \angle N(1)-Hg-I(1) = 101.72(6) $^\circ$; \angle N(1)-Hg-I(2) = 106.19(6) $^\circ$]. Moreover, the molecules of **3** are interlinked through Hg \cdots O [2.949(3) and 2.844(3) Å] and I \cdots I [3.8791(4) Å] interactions, leading to the formation of a 2D supramolecular layer, Figure 4b. The I \cdots I distance of 3.8791(4) Å is significantly shorter than the sum of two van der Waals radii of the iodo atom, which is 3.96 Å.

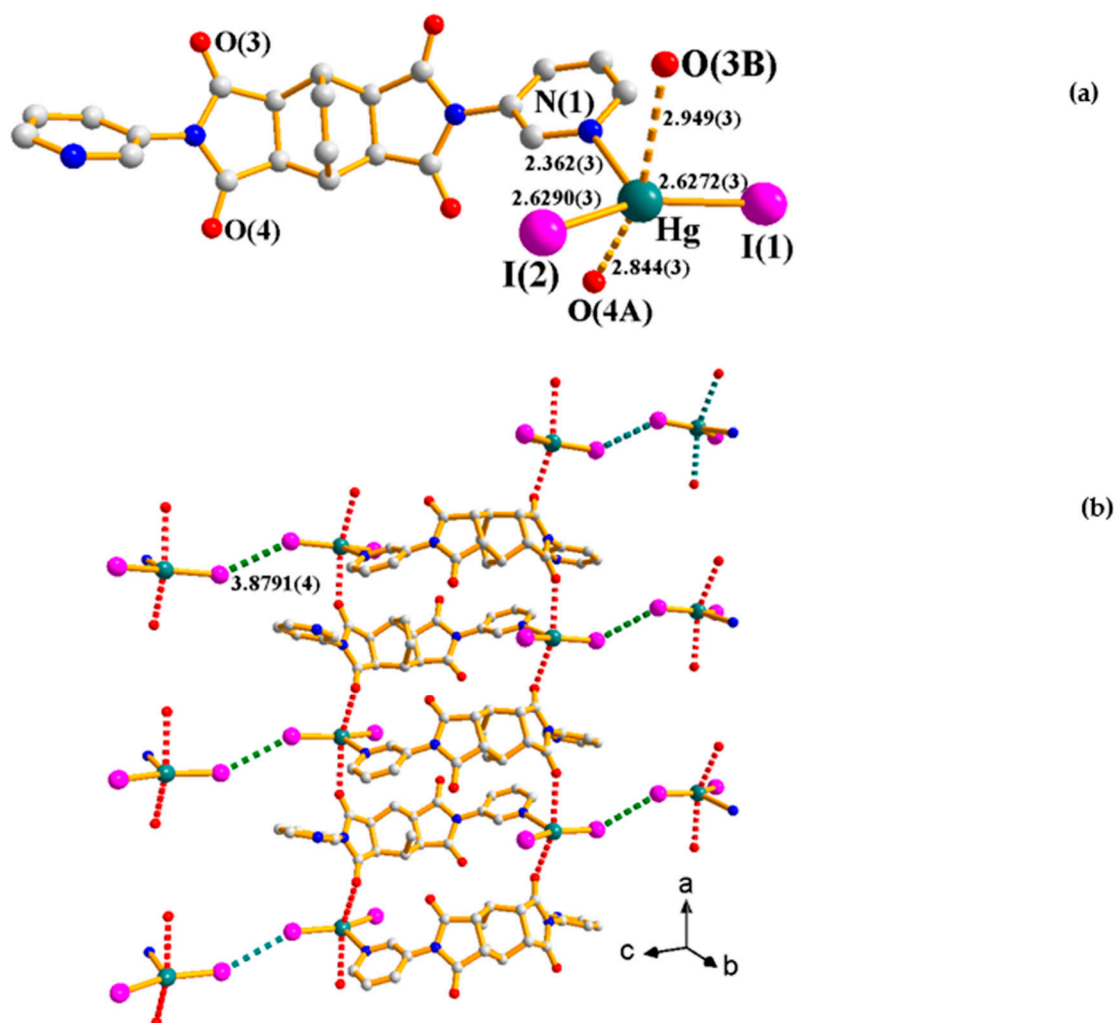


Figure 4. (a) Coordination environment of Hg(II) ion in **3**. Symmetry transformations used to generate equivalent atoms: (A) $-x + 1, -y + 1, -z + 2$; (B) $-x + 2, -y + 1, -z + 2$. (b) A drawing showing the 2D supramolecular layer.

2.4. Crystal Structures of **4–6**

Complexes **4–6** are isomorphous, and their crystals conform to monoclinic space group $C2/c$ with one Hg(II) cation, two halide anions, and one L^2 ligand in the asymmetric unit. Figure 5 shows a representative drawing for the dinuclear structures of **4–6** ($X = Cl$, **4**; Br , **5**; I , **6**). The coordination environment of the Hg(II) metal center is four-coordinated by two nitrogen atoms from two L^2 ligands and two halide anions, resulting in a distorted tetrahedral geometry ($\tau_4 = 0.71$ for **1**; 0.73 for **2**; 0.75 for **3**). Table 1 lists the selected bond distances and angles for **4–6**. The dihedral angles between the two phenyl rings of L^2 are 59.24 , 61.25 , and 63.300 , respectively. While the Hg-X distances and the dihedral angles increase from **4** to **6**, the X-Hg-X angles decrease, showing the size effect of the halide anions. Moreover, the molecules of the dinuclear complexes **4–6** are linked by the intermolecular C-H \cdots O (H \cdots O = 2.509 – 2.539 Å, \angle C-H \cdots O = 113.9 – 143.8° for **4**; H \cdots O = 2.522 – 2.587 Å, \angle C-H \cdots O = 114.2 – 137.0° for **5**; H \cdots O = 2.532 – 2.638 Å, \angle C-H \cdots O = 113.9 – 132.7° for **6**), and **5–6** are also linked by the intermolecular C-H \cdots X (H \cdots Br = 3.069 , 3.115 Å, \angle C-H \cdots Br = 130.3 , 118.5° ; H \cdots I = 3.186 , 3.281 Å, \angle C-H \cdots I = 132.5 , 123.2°) interactions, resulting in 3D supramolecular structures, Figures S1–S3.

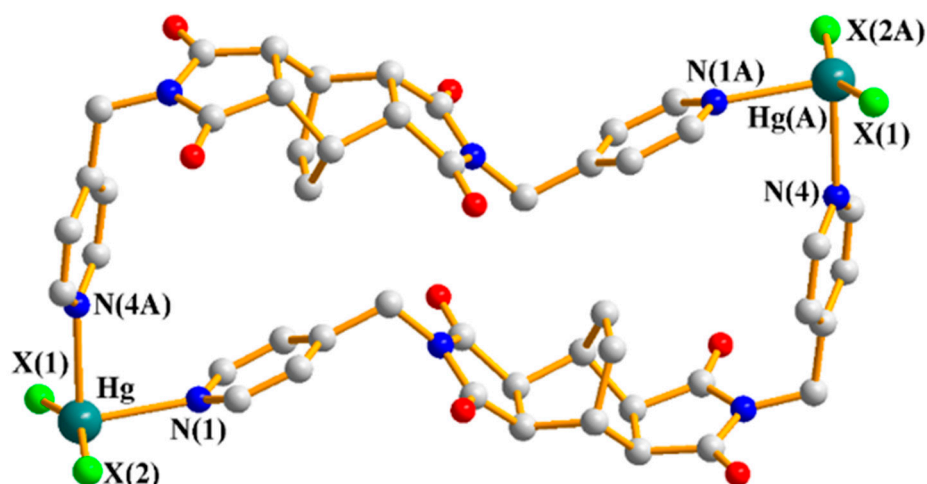


Figure 5. A representative drawing showing the dinuclear structures of **4** (X = Cl), **5** (X = Br), and **6** (X = I). Symmetry transformations used to generate equivalent atoms: (A) $-x + 1/2, -y + 1/2, -z + 1$ for **4**, $-x + 1/2, -y + 3/2, -z + 1$ for **5** and **6**.

Table 1. Selected bond lengths (Å) and angles (°) for complexes **4** (X = Cl), **5** (X = Br), and **6** (X = I).

	4	5	6
Hg-N(1)	2.452(4)	2.503(4)	2.507(3)
Hg-N(4A)	2.510(4)	2.453(4)	2.459(3)
Hg-X(1)	2.3554(14)	2.4681(8)	2.6386(4)
Hg-X(2)	2.3461(15)	2.4670(8)	2.6322(4)
\angle N(1)-Hg-N(4A)	84.27(13)	84.31(15)	83.92(12)
\angle N(1)-Hg-X(1)	100.98(11)	98.54(10)	99.37(8)
\angle N(1)-Hg-X(2)	97.22(10)	97.14(11)	100.10(9)
\angle N(4A)-Hg-X(1)	97.47(10)	101.43(12)	102.67(9)
\angle N(4A)-Hg-X(2)	94.91(10)	99.21(12)	100.18(9)
\angle X(1)-Hg-X(2)	158.88(5)	155.15(2)	151.300(12)

2.5. Crystal Structures of 7–9

Single-crystal X-ray diffraction analysis reveals that the isomorphous complexes **7–9** are crystallized in the monoclinic space group $P2_1/c$ with one Hg(II) ion, one L^3 ligand, two halide anions, and one co-crystallized water molecule in each asymmetric unit. Figure 6a depicts a representative drawing showing the coordination environment of the Hg(II) centers. The central Hg (II) ions are four-coordinated by two pyridyl nitrogen atoms from two L^3 ligands and two halide anions, resulting in tetrahedral geometries, which are further linked by the L^3 ligands to form 1D zigzag chains, Figure 6b. Table 2 lists the selected bond distances and angles for **7–9**. While the Hg-N distances are similar, the Hg-X distances increase from Cl to I and the X-Hg-X angles decrease. Moreover, the zigzag chains of **7–9** are linked by the intermolecular C-H...O (H...O = 2.392, 2.479 Å, \angle C-H...O = 136.3, 141.6° for **7**; H...O = 2.395, 2.522 Å, \angle C-H...O = 140.5, 142.8° for **8**; H...O = 2.456, 2.599 Å, \angle C-H...O = 143.3, 147.9° for **9**) and the intermolecular C-H...X (H...Cl = 2.851, 2.878 Å, \angle C-H...Cl = 150.7, 131.6°; H...Br = 2.916, 2.979 Å, \angle C-H...Br = 158.2, 132.9°; H...I = 3.065, 3.154 Å, \angle C-H...I = 143.3, 133.0°) interactions, as well as the N-H...O (H...O = 1.990 Å, \angle N-H...O = 161.1° for **7**; H...O = 2.059 Å, \angle N-H...O = 159.4° for **8**; H...O = 2.160 Å, \angle N-H...O = 156.7° for **9**) interactions with the amide oxygen atoms, resulting in 3D supramolecular structures, Figures S4–S6.

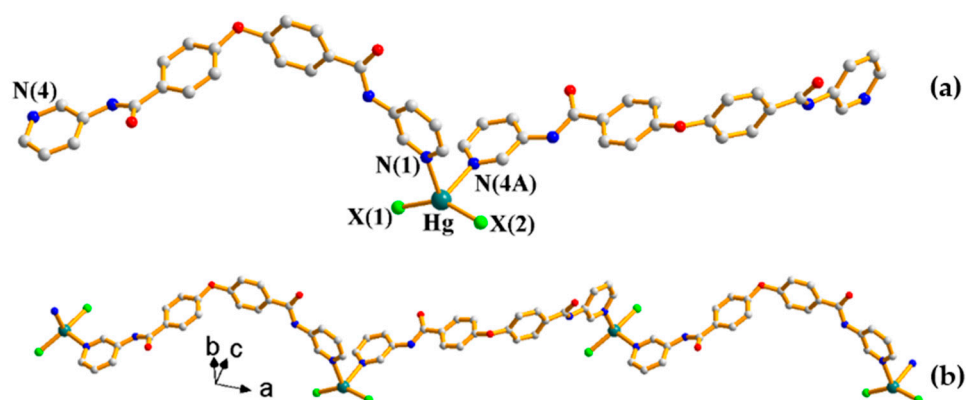


Figure 6. (a) A representative drawing showing the coordination environment about the Hg(II) ion for 7–9. Symmetry transformations used to generate equivalent atoms: (A) $x + 1, -y + 3/2, z + 1/2$. (b) A drawing showing the 1D linear chain.

Table 2. Selected bond distance (Å) and bond angles (°) for 7 (X = Cl), 8 (X = Br), and 9 (X = I).

	7	8	9
Hg-X(1)	2.3374(11)	2.4771(13)	2.6270(6)
Hg-X(2)	2.3858(10)	2.5213(12)	2.6732(6)
Hg-N(4A)	2.413(3)	2.419(9)	2.435(5)
Hg-N(1)	2.418(3)	2.388(8)	2.405(5)
$\angle X(1)\text{-Hg-X}(2)$	147.79(4)	143.29(5)	139.976(18)
$\angle X(1)\text{-Hg-N}(4A)$	105.38(8)	106.6(2)	107.22(12)
$\angle X(2)\text{-Hg-N}(4A)$	97.52(7)	99.1(2)	100.84(12)
$\angle X(1)\text{-Hg-N}(1)$	104.26(7)	106.4(2)	106.63(11)
$\angle X(2)\text{-Hg-N}(1)$	99.16(7)	100.2(2)	102.16(11)
$\angle N(4A)\text{-Hg-N}(1)$	87.10(10)	88.0(3)	88.18(18)

Some additional parameters were manipulated to probe the structural differences in the isomorphous 7–9, where distances $d1$ and $d2$ are distances from the bridging oxygen atom to the two Hg(II) ions and $d3$ is the distance between the two Hg(II) ions bridged by the L ligand, and angles $\theta1$, $\theta2$, and $\theta3$ are the dihedral angles differences (Figure 7 and Table 3). The dihedral angles $\theta2$ and $\theta3$ increased from 1 to 3, while the $\theta1$ values are in a reverse order, indicating the effect of the size of the halide anion on the structures.

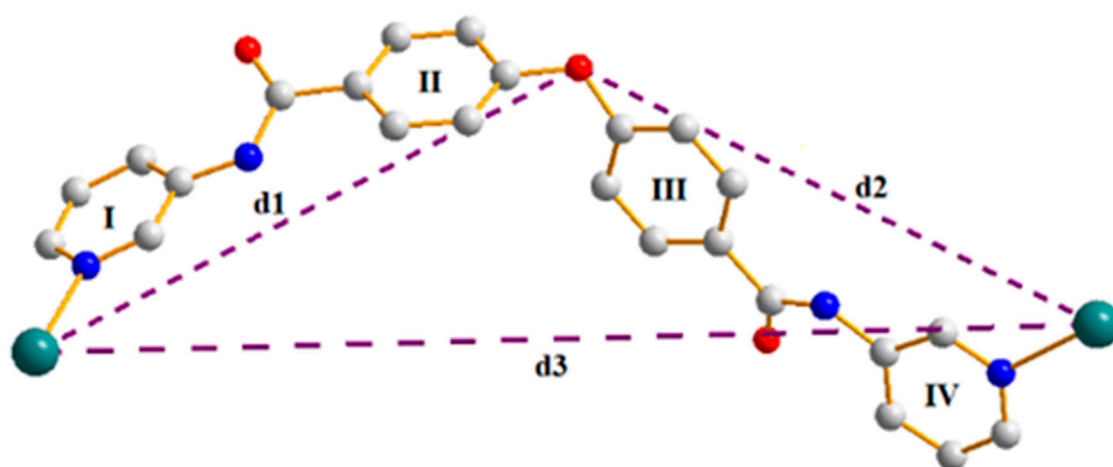


Figure 7. A schematic diagram defining the distances and the dihedral angle.

Table 3. Comparison of angles and distances for complexes 7–9.

	d1 (Å)	d2 (Å)	d3 (Å)	θ1 (°)	θ2 (°)	θ3 (°)	C-O-C
7	11.05	11.50	19.80	21.75	77.79	2.11	118.3(2)
8	11.06	11.47	19.60	19.52	81.09	3.21	117.3(7)
9	11.06	11.40	19.41	16.89	84.51	5.94	117.3(4)

2.6. Effect of Halide Anion and Ligand Type on Structural Diversity

The structural types of complexes 1–9 are listed in Table 4. While complexes 1–3 containing rigid-bulky L^1 display different structures that are subject to the nature of the halide anion, the structural diversity of the flexible-bulky L^2 -based 4–6 and the angular L^3 -based 7–9 is independent of the nature of the halide anion. The halide anions play different structure-determining roles in 1–9 containing different bpba ligands. The halide anion effect on the structural types of the Hg(II) CPs is thus subject to the identity of the bpba ligand.

Table 4. Structural types of 1–9.

Complex	Structure
$[HgCl_2] \cdot 2L^1$, 1	1D supramolecular chain
$[HgBr_2(L^1)]_n$, 2	1D zigzag chain
$[HgI_2(L^1)]$, 3	2D supramolecular layer
$[Hg_2Cl_4(L^2)_2]$, 4	Dinuclear metallocycle
$[Hg_2Br_4(L^2)_2]$, 5	Dinuclear metallocycle
$[Hg_2I_4(L^2)_2]$, 6	Dinuclear metallocycle
$\{[HgCl_2(L^3)] H_2O\}_n$, 7	1D zigzag chain
$\{[HgBr_2(L^3)] H_2O\}_n$, 8	1D zigzag chain
$\{[HgI_2(L^3)] H_2O\}_n$, 9	1D zigzag chain

2.7. Luminescence Properties

Complexes 7–9 that contain d^{10} Hg(II) ions and organic ligand L^3 with a large π -conjugated system may exhibit fluorescent properties [19]. Therefore, their solid-state emission spectra were examined at room temperature, as shown in Figure 8 and Table 5. The free L^3 ligand shows an emission at 430 nm upon excitation at 330 nm, which could be due to the $n \rightarrow \pi^*$ or $\pi \rightarrow \pi^*$ transitions, while complexes 7–9 exhibit emission bands at 420, 416, and 400 nm, respectively. Due to the d^{10} electronic configuration of the Hg(II) metal ion that hardly undergoes either oxidation or reduction, the emissions of 7–9 may thus result from the organic linkers and are attributable to $n \rightarrow \pi^*$ or $\pi \rightarrow \pi^*$ transitions [20]. Noticeably, the emission wavelengths of 7–9 are similar with decreasing intensities from Cl, Br, to I, indicating the heavy atom effect of the halide anions [21]. It is noted that no detectable emission can be found for the L^1 , L^2 and their complexes 1–6, which can be ascribed to the different natures of L^1 , L^2 , and L^3 .

Table 5. Luminescent properties of 7–9.

Compound	Excitation λ_{ex} (nm)	Emission λ_{em} (nm)
L^3	330	430
7	325	420
8	326	416
9	316	400

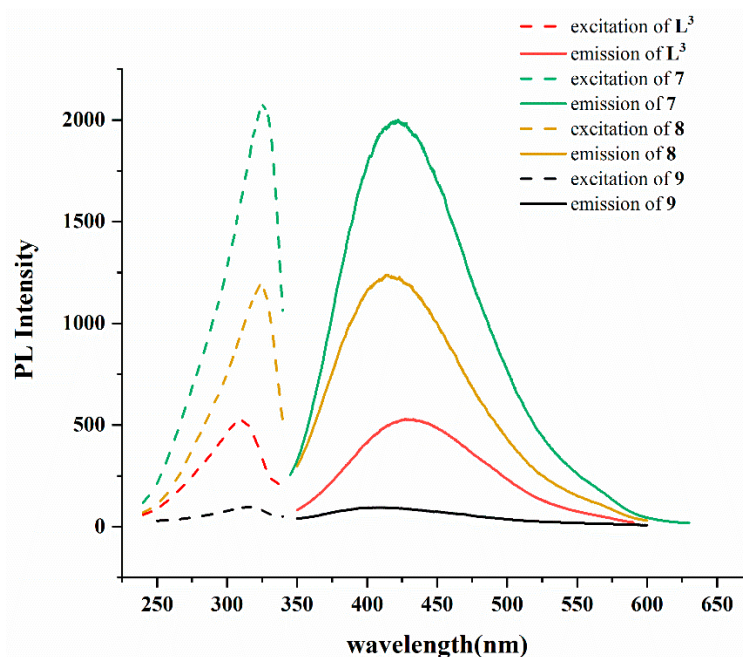


Figure 8. Excitation and emission spectra of complexes 7–9 and L³.

2.8. Mechanochemical Synthesis and Stability of Complexes 7–9

To obtain complexes 7–9 efficiently, we studied their mechanochemical synthesis. Manual grinding of mercury(II) halide salts with L³ in methanol/H₂O or ethanol/H₂O afforded complexes 7–9, which were verified by characterization using PXRD. As shown in Figures S7–S9, the PXRD patterns of the samples prepared using the solvothermal reactions and mechanochemical reactions matched quite well, indicating the bulk purities of 7–9. The PXRD patterns of the mechanochemical products were comparatively broad, most probably due to the fact that mechanochemical products generally have lower crystallinity compared with the solvothermal product. Additionally, the mechanochemical method was only successful in the MeOH/H₂O and EtOH/H₂O solvent systems, while in various solvents such as pure H₂O, CH₂Cl₂, and MeCN, different products were obtained, indicating the solvent selectivity of complexes 7–9 (Figures S10–S12). The stability of complexes 7–9 was studied by immersing them into H₂O, EtOH, MeOH, CH₂Cl₂, and MeCN, respectively, for up to 7 days. Complexes 7–9 were then filtered and dried under vacuum and their PXRD patterns were measured. Figures S13–S15 show that the experimental PXRD patterns matched well with the simulated ones, indicating complexes 7–9 are stable in these solvents.

2.9. Halide Anion Effect on Metal Sensing

Complexes 7 and 8 provide a unique opportunity to investigate the effect of the halide anion on metal sensing. For the investigations, 25 mg samples of 7 and 8, respectively, was immersed into 10 mL aqueous solutions of nitrate salts M(NO₃)_x or acetate salts M(OAc)_x (M = Ag⁺, Cd²⁺, Co²⁺, Mn²⁺, Ni²⁺, Mg²⁺, Cu²⁺, and Fe³⁺). After 10 h, the solids were filtered and their emission spectra were measured. As shown in Figures S16–S18, remarkable luminescence quenching of about 91% for 7 and 90% for 8 were found in the detection of Fe³⁺ ions. To further explore the quenching effect of Fe³⁺ ions, the sensing dependence of luminescence intensity on the concentration of Fe³⁺ was investigated by immersing finely ground samples (25 mg) of 7 or 8 into Fe³⁺ aqueous solutions with various concentrations (0.1 mM–1 mM) for 10 h. Figures S19 and S20 show that the emission intensities were getting lower and almost completely quenched upon increasing the concentration of Fe³⁺. Quantitatively, the quenching capacity of the Fe³⁺ ion can be rationalized by the Stern–Volmer equation: $I_0/I = 1 + K_{sv} \times [Q]$, where [Q] is the concentration of Fe³⁺, K_{sv} is the quenching constant, and I₀ and I are the emission intensities

in the absence and presence of Fe^{3+} , respectively [22]. As demonstrated in Figure 9, the titration curves for Fe^{3+} ions in **7** and **8** are virtually linear at low concentrations, which gave the linear correlation coefficient (R^2) of 0.9714 for **7** and 0.9525 for **8**, respectively, while the S-V curves at higher concentrations became nonlinear, affording Stern–Volmer constants (K_{SV}) of $2.48 \times 10^4 \text{ M}^{-1}$ for **7** and $1.2 \times 10^4 \text{ M}^{-1}$ for **8**, respectively.

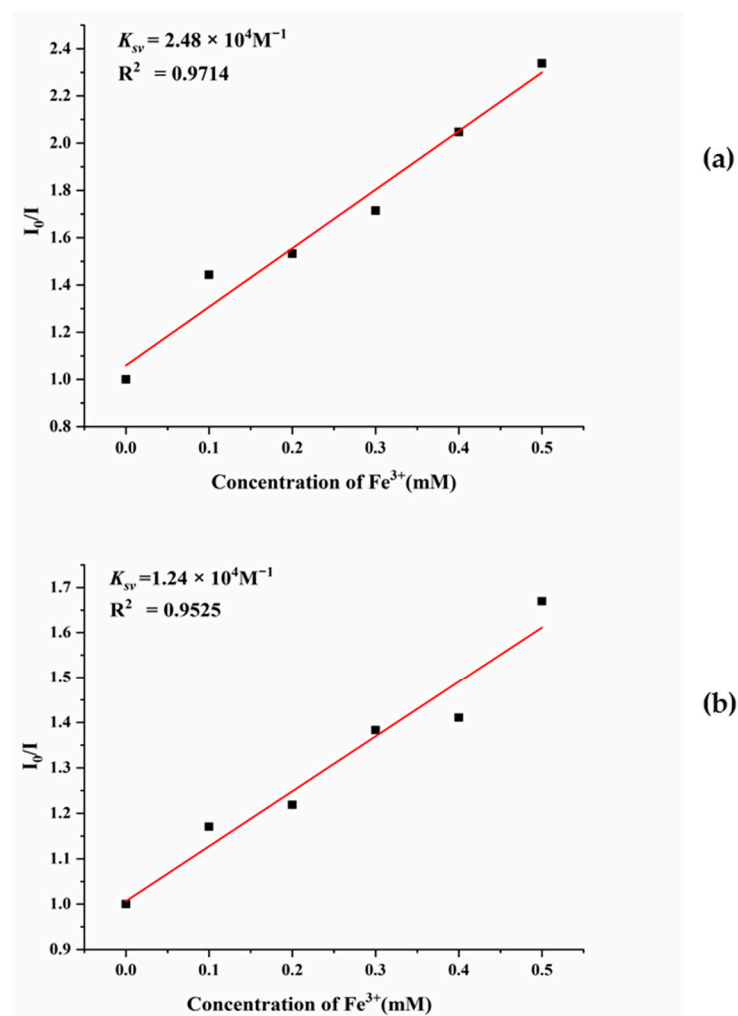


Figure 9. The Stern–Volmer plot of I_0/I versus Fe^{3+} ions' concentration for (a) **7** ($\lambda_{\text{ex}} = 325 \text{ nm}$) and (b) **8** ($\lambda_{\text{ex}} = 326 \text{ nm}$).

Furthermore, the detection limits were calculated according to the standard equation $3\sigma/k$, where σ is the standard deviation from the blank measurements and k is the absolute value of the calibration curve at a lower concentration [23], giving 7.38 and 24 μM for **7** and **8**, respectively. The recyclability test showed no significant changes in the PXRD patterns (Figures 10 and 11), and the luminescence intensities (Figures S21 and S22) for five regeneration cycles were consistent, indicating the reusability of **7** and **8** as sensing materials toward Fe^{3+} . This demonstrates that the luminescence quenching is not due to the framework collapse of **7** and **8**, but upon the interactions with the Fe^{3+} ions. The use of Hg(II) CPs for sensing is rarely seen, and a 1D double-chain $\{[\text{Hg}(\text{L})_2] \cdot (\text{ClO}_4)_2\}_n$ ($\text{L} = 1,3,5$ -tris(benzimidazolylmethyl)benzene) has been reported to show multistimuli-responsive photoluminescence sensing properties toward anions, solvents, and nitroaromatic compounds [24].

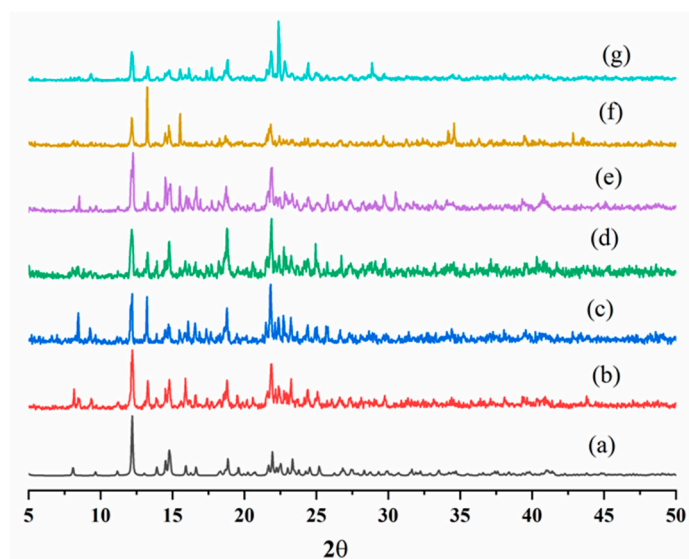


Figure 10. PXRD patterns before and after treatments with Fe^{3+} ions for 7. (a) Simulated, (b) experimental, (c) 1st cycle, (d) 2nd cycle, (e) 3rd cycle, (f) 4th cycle, and (g) 5th cycle.

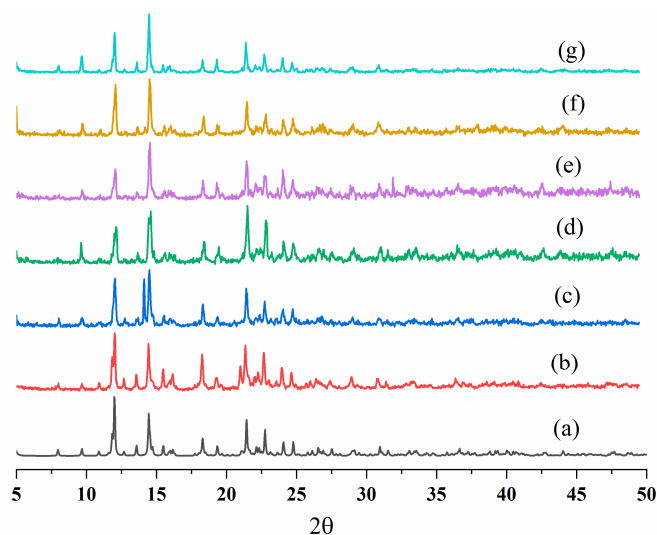


Figure 11. PXRD patterns before and after treatments with Fe^{3+} ions for 8. (a) Simulated, (b) experimental, (c) 1st cycle, (d) 2nd cycle, (e) 3rd cycle, (f) 4th cycle, and (g) 5th cycle.

Several mechanisms for luminescence quenching such as framework collapse, cation exchange, and interactions between the incoming metal ion and the organic linker that result in competitive absorption of the excitation energies have been suggested [25]. Since the quenching of the luminescence is not due to the framework collapse, the interactions between Fe^{3+} ions and complexes 7 and 8 are the main reasons leading to the luminescence quenching [26]. The UV-Vis absorption spectrum of Fe^{3+} in aqueous solution and the corresponding excitation and emission spectra of complexes 7 and 8 are shown in Figures S23 and S24, respectively. Partial overlaps between the absorption spectrum of the Fe^{3+} ion and the excitation spectra of complexes 7 and 8 are observed, indicating that the excitation energies of 7 and 8 can be partially absorbed by the Fe^{3+} ions, and the luminescence quenching can most probably be ascribed to competitive energy absorption [25].

Moreover, the K_{SV} values, $2.48 \times 10^4 \text{ M}^{-1}$ for 7 and $1.2 \times 10^4 \text{ M}^{-1}$ for 8, may indicate that the Fe^{3+} ion shows a better quenching effect to the chloride complex 7. In addition to the possible interactions between the metal ions and the amide carbonyl oxygen atoms of the L^3 ligands [26], the halide anions of 7 and 8 may play an important role in determining

the quenching effect. It is well known that the atomic radius of Cl^- is shorter than that of Br^- , and comparatively, Cl^- can be regarded as a harder Lewis base than Br^- . Since Fe^{3+} is a hard Lewis acid and interacts stronger with the Cl^- anion, the larger quenching effect to **7** is attributable to the formation of the stronger $\text{Hg-Cl}\cdots\text{Fe}^{3+}$ interaction upon the addition of the Fe^{3+} ion to complex **7**. The different quenching effect exerted by the Fe^{3+} ion may thus be ascribed to the different $\text{Hg-X}\cdots\text{Fe}^{3+}$ ($\text{X} = \text{Cl}$ and Br) interactions. Energy dispersive X-ray (EDX) analysis of complexes **7–8** was performed after Fe^{3+} sensing (Figures S25 and S26), confirming the Fe^{3+} uptake of **7–8**.

3. Materials and Methods

3.1. General Procedures

Elemental analyses of (C, H, N) were performed on a PE 2400 series II CHNS/O (PerkinElmer Instruments, Shelton, CT, USA) or an Elementar Vario EL-III analyzer (Elementar Analysensysteme GmbH, Hanau, Germany). Infrared spectra were obtained from a JASCO FT/IR-460 plus spectrometer with pressed KBr pellets (JASCO, Easton, MD, USA). Powder X-ray diffraction patterns were carried out with a Bruker D8-Focus Bragg–Brentano X-ray powder diffractometer equipped with a $\text{CuK}\alpha$ ($\lambda_\alpha = 1.54178 \text{ \AA}$) sealed tube (Bruker Corporation, Karlsruhe, Germany). The UV-Vis spectrum was performed on a UV-2450 spectrophotometer (Dongguan Hongcheng Optical Products Co., Dongguan, China). Emission spectra were determined with a Hitachi F-4500 fluorescence spectrophotometer (Hitachi, Tokyo, Japan). Energy dispersive X-ray (EDX) analysis was performed by using a JEOL JSM-7600F Ultra-High Resolution Schottky Field Emission Scanning Electron Microscope with Oxford Xmax80 energy dispersive X-ray spectrometer (JEOL, Ltd., Tokyo, Japan).

3.2. Materials

The reagents HgCl_2 and HgBr_2 were purchased from Acros Organics (Thermo Fisher Scientific, NJ, USA) and HgI_2 from Aldrich Chemistry Co. (Milwaukee, WI, USA). The solvents CH_3OH (99.5%) and $\text{CH}_3\text{CH}_2\text{OH}$ (99.5%) were purchased from Echo Chemical Co., Ltd. (Toufen, Miaoli, Taiwan). The L^1 , L^2 , and L^3 ligands were prepared according to published procedures with slight modification [27–29].

3.3. Preparations

3.3.1. $[\text{HgCl}_2]\cdot 2\text{L}^1$, **1**

A mixture of HgCl_2 (0.027 g, 0.10 mmol), L^1 (0.040 g, 0.10 mmol), and 10 mL EtOH was sealed in a 23 mL Teflon-lined stainless steel autoclave, which was heated under autogenous pressure to 120 °C for two days, and then, the reaction system was cooled to room temperature at a rate of 2 °C per hour. The colorless crystals suitable for single-crystal X-ray diffraction were obtained. Yield: 0.043 g (40%). Anal. Calcd for $\text{C}_{44}\text{H}_{32}\text{Cl}_2\text{HgN}_8\text{O}_8$ ($M_W = 1072.26$): C, 49.29; H, 3.01; N, 10.45%. Found: C, 48.89; H, 2.88; N, 10.33%. FT-IR (cm^{-1}): 3457 (s), 2363 (w), 2342 (w), 1715 (s), 1639 (m), 1566 (m), 1482 (m), 1429 (m), 1384 (s), 1178 (m), 1098 (w), 1048 (w), 1028 (w), 779 (m), 702 (m), 680 (m), 628 (m).

3.3.2. $[\text{HgBr}_2(\text{L}^1)]_n$, **2**

Complex **2** was prepared by using similar procedures for **1**, except that HgBr_2 (0.036 g, 0.10 mmol), L^1 (0.040 g, 0.10 mmol), and 10 mL MeOH were used. Colorless crystals were obtained. Yield: 0.073 g (96%). Anal. Calcd for $\text{C}_{22}\text{H}_{16}\text{Br}_2\text{HgN}_4\text{O}_4$ ($M_W = 760.78$): C, 34.74; H, 2.11; N, 7.37%. Found: C, 34.75; H, 1.98; N, 7.37%. IR (cm^{-1}): 3588 (m), 2361 (m), 2340 (m), 1708 (s), 1484 (m), 1434 (m), 1374 (m), 1316 (w), 1232 (w), 1200 (m), 1080 (w), 1026 (w).

3.3.3. $[\text{HgI}_2(\text{L}^1)]$, **3**

Complex **3** was prepared by using similar procedures for **1**, except that HgI_2 (0.045 g, 0.10 mmol), L^1 (0.040 g, 0.01 mmol), and 10 mL MeOH were used. Colorless crystals were

obtained. Yield: 0.044 g (51%). Anal. Calcd for $C_{22}H_{16}HgI_2N_4O_4$ ($M_W = 854.78$): C, 30.91; H, 1.89; N, 6.55%. Found: C, 30.76; H, 1.84; N, 6.49%. FT-IR (cm^{-1}): 3442 (s), 1722 (m), 1691 (m), 1638 (m), 1483 (w), 1430 (w), 1373 (m), 1201 (m), 1169 (w), 1050 (m), 776 (w), 729 (w), 695 (w), 680 (w), 575 (w).

3.3.4. $[Hg_2Cl_4(L^2)]_2$, **4**

Complex **4** was prepared by using similar procedures for **1**, except that $HgCl_2$ (0.027 g, 0.10 mmol), L^2 (0.043 g, 0.10 mmol), and 10 mL MeOH were used. Colorless crystals were obtained. Yield: 0.053 g (76%). Anal. Calcd for $C_{48}H_{40}Cl_4Hg_2N_8O_8$ ($M_W = 1399.86$): C, 41.14; H, 2.86; N, 8.00%. Found: C, 40.75; H, 2.89; N, 7.91%. IR (cm^{-1}): 3074 (w), 2939 (w), 2361 (w), 1768 (m), 1703 (s), 1612 (m), 1565 (w), 1429 (m), 1400 (m), 1347 (m), 1318 (m), 1220 (w), 1171 (m), 1108 (w), 1010 (w), 914 (m), 877 (w), 800 (w), 771 (m), 731 (w), 667 (w), 633 (m), 585 (w), 492 (m).

3.3.5. $[Hg_2Br_4(L^2)]_2$, **5**

Complex **5** was prepared by following the similar procedures for **4**, except that $HgBr_2$ (0.036 g, 0.10 mmol) was used. Colorless crystals were obtained. Yield: 0.055 g (70%). Anal. Calcd for $C_{48}H_{40}Br_4Hg_2N_8O_8$ ($M_W = 1577.66$): C, 36.55; H, 2.54; N, 7.11%. Found: C, 36.69; H, 2.39; N, 7.08%. IR (cm^{-1}): 3072 (w), 2933 (w), 2361 (w), 1768 (w), 1702 (s), 1611 (m), 1565 (w), 1429 (m), 1399 (m), 1346 (m), 1317 (m), 1219 (w), 1170 (m), 1107 (w), 1011 (w), 915 (m), 876 (w), 798 (w), 770 (m), 731 (w), 667 (w), 634 (m), 586 (w), 492 (m).

3.3.6. $[Hg_2I_4(L^2)]_2$, **6**

Complex **6** was prepared by following the similar procedures for **4**, except that HgI_2 (0.045 g, 0.10 mmol) was used. Colorless crystals were obtained. Yield: 0.039 g (44%). Anal. Calcd for $C_{48}H_{40}Hg_2I_4N_8O_8$ ($M_W = 1765.66$): C, 32.58; H, 2.26; N, 6.33%. Found: C, 32.72; H, 2.16; N, 6.31%. IR (cm^{-1}): 3736 (w), 3567 (w), 3067 (w), 2967 (w), 2927 (w), 2362 (m), 2340 (w), 1942 (w), 1768 (m), 1701 (s), 1611 (m), 1565 (w), 1427 (m), 1396 (s), 1344 (m), 1316 (m), 1217 (m), 1169 (m), 1070 (m), 1009 (m), 914 (m), 875 (m), 796 (m), 769 (m), 729 (m), 696 (w), 667 (m).

3.3.7. $\{[HgCl_2(L^3)] \cdot H_2O\}_n$, **7**

Complex **7** was prepared by using similar procedures for **1**, except $HgCl_2$ (0.028 g, 0.10 mmol), L^3 (0.043 g, 0.10 mmol) in 8 mL EtOH, and 2 mL H_2O were used. Colorless crystals were obtained. Yield: 0.057 g (81%). Anal. Calcd for $C_{24}H_{20}Cl_2HgN_4O_4$ ($M_W = 699.93$): C, 41.18; H, 2.88; N, 8.00%. Found: C, 41.02; H, 2.28; N, 7.56%. IR (cm^{-1}): 3292 (s), 3046 (w), 1920 (m), 1660 (s), 1535 (s), 1505 (s), 1496 (s), 1414 (m), 1231 (s), 1170 (m), 1116 (s), 1097 (m), 1051 (w), 944 (m), 863 (m), 843 (m), 803 (m), 757 (m), 698 (m), 643 (w), 590 (m), 518 (w), 499 (w).

3.3.8. $\{[HgBr_2(L^3)] \cdot H_2O\}_n$, **8**

Complex **8** was prepared by following the similar procedures for **7**, except $HgBr_2$ (0.036 g, 0.10 mmol) was used. Colorless crystals were obtained. Yield: 0.058 g (74%). Anal. Calcd for $C_{24}H_{20}Br_2HgN_4O_4$ ($M_W = 788.85$): C, 36.54; H, 2.55; N, 7.10%. Found: C, 36.49; H, 2.88; N, 7.04%. IR (cm^{-1}): 3280 (s), 3046 (w), 1914 (m), 1656 (s), 1539 (s), 1498 (s), 1479 (s), 1416 (m), 1233 (s), 1174 (m), 1109 (s), 1051 (m), 937 (m), 869 (m), 844 (m), 804 (m), 758 (m), 694 (m), 638 (w), 592 (m), 532 (w), 493 (w).

3.3.9. $\{[HgI_2(L^3)] \cdot H_2O\}_n$, **9**

Complex **9** was prepared by following the similar procedures for **7**, except HgI_2 (0.045 g, 0.10 mmol) was used. Colorless crystals were obtained. Yield: 0.046 g (52%). Anal. Calcd for $C_{24}H_{20}HgI_2N_4O_4$ ($M_W = 882.83$): C, 32.65; H, 2.28; N, 6.34%. Found: C, 33.18; H, 1.99; N, 6.06%. IR (cm^{-1}): 3297 (s), 3057 (w), 1920 (m), 1653 (s), 1544 (s), 1496 (s), 1480 (s),

1414 (m), 1228 (s), 1171 (m), 1115 (s), 1052 (m), 1048 (w), 942 (m), 866 (m), 842 (m), 803 (m), 759 (m), 697 (m), 636 (w), 585 (m), 535 (w), 499 (w).

3.4. Powder X-ray Analysis

In order to check the phase purity of the product, powder X-ray diffraction (PXRD) experiments were carried out for complexes 1–9. As shown in Figures S7–S9 and S27–S32, the peak positions of the experimental and simulated PXRD patterns were in good agreement with each other, indicating the bulk purities.

3.5. X-ray Crystallography

Single-crystal X-ray diffraction data for complexes 1–9 were collected on a Bruker AXS SMART APEX II CCD diffractometer with graphite-monochromated MoK α ($\lambda_{\alpha} = 0.71073 \text{ \AA}$) radiation at 296 K [30]. Data reduction and absorption correction were performed by using standard methods with well-established computational procedures [31]. Some of the heavier atoms were located by the direct or Patterson method, and the remaining atoms were found in a series of Fourier maps and least-squares refinements, while the hydrogen atoms were added by using the HADD command in SHELXTL. Basic information pertaining to crystal parameters and structure refinement is listed in Table 6.

Table 6. Crystallographic data for 1–9.

Compound	1	2	3
Formula	C ₄₄ H ₃₂ Cl ₂ HgN ₈ O ₈	C ₂₂ H ₁₆ Br ₂ HgN ₄ O ₄	C ₂₂ H ₁₆ HgI ₂ N ₄ O ₄
Formula weight	1072.26	760.80	854.78
Crystal system	Triclinic	Triclinic	Triclinic
Space group	<i>P</i> $\bar{1}$	<i>P</i> $\bar{1}$	<i>P</i> $\bar{1}$
a, \AA	8.7814(14)	6.80779(8)	9.7275(5)
b, \AA	10.5498(16)	11.83139(14)	11.5101(8)
c, \AA	10.9631(16)	14.71857(16)	12.4521(7)
α , $^{\circ}$	85.121(4)	80.4699(6)	106.3362(18)
β , $^{\circ}$	74.166(4)	85.6414(6)	98.0437(13)
γ , $^{\circ}$	81.889(4)	81.8897(6)	114.9454(11)
V, \AA^3	966.2(3)	1155.78(2)	1158.30(12)
Z	1	2	2
D _{calc} , Mg/m ³	1.843	2.186	2.451
F(000)	530	716	788
μ (Mo K α), mm ⁻¹	4.192	10.153	9.347
Range (2 θ) for data collection, deg	3.86 \leq 2 θ \leq 56.73	3.52 \leq 2 θ \leq 56.60	3.57 \leq 2 θ \leq 52.00
Independent reflections	4816 [R(int) = 0.0350]	5727 [R(int) = 0.0298]	4540 [R(int) = 0.0317]
Data/restraints/parameters	4816/0/286	5727/0/298	4540/0/298
quality-of-fit indicator ^c	1.088	1.070	1.029
Final R indices [I > 2 σ (I)] ^{a,b}	R1 = 0.0142, wR2 = 0.0368	R1 = 0.0289, wR2 = 0.0696	R1 = 0.0158, wR2 = 0.0396
R indices (all data)	R1 = 0.0142, wR2 = 0.0368	R1 = 0.0327, wR2 = 0.0714	R1 = 0.0161, wR2 = 0.0397

Table 6. Cont.

Compound	4	5	6
Formula	C ₄₈ H ₄₀ Cl ₄ Hg ₂ N ₈ O ₈	C ₄₈ H ₄₀ Br ₄ Hg ₂ N ₈ O ₈	C ₄₈ H ₄₀ Hg ₂ I ₄ N ₈ O ₈
Formula weight	1399.86	1577.70	1765.66
Crystal system	Monoclinic	Monoclinic	Monoclinic
Space group	C2/c	C2/c	C2/c
a, Å	25.8153(6)	26.208(2)	26.7552(5)
b, Å	7.0635(2)	7.1272(7)	7.2351(1)
c, Å	27.1652(7)	27.046(3)	27.0340(5)
α, °	90	90	90
β, °	97.5487(12)	97.866(5)	98.0783(9)
γ, °	90	90	90
V, Å ³	4910.5(2)	5004.3(8)	5181.22(15)
Z	4	4	4
D _{calc} , Mg/m ³	1.893	2.094	2.264
F(000)	2704	2992	3280
μ (Mo Kα), mm ⁻¹	6.525	9.383	8.362
Range (2θ) for data collection, deg	3.024 ≤ 2θ ≤ 56.656	3.04 ≤ 2θ ≤ 56.89	3.044 ≤ 2θ ≤ 56.678
Independent reflections	6126 [R(int) = 0.0372]	6265 [R(int) = 0.0588]	6439 [R(int) = 0.0371]
Data/restraints/parameters	6126/0/316	6265/0/298	6439/0/317
quality-of-fit indicator ^c	1.059	1.025	1.033
Final R indices [I > 2σ(I)] ^{a,b}	R1 = 0.0380, wR2 = 0.0951	R1 = 0.0397, wR2 = 0.0815	R1 = 0.0294, wR2 = 0.0674
R indices (all data)	R1 = 0.0506, wR2 = 0.1001	R1 = 0.0717, wR2 = 0.0904	R1 = 0.0363, wR2 = 0.0706
Compound	7	8	9
Formula	C ₂₄ H ₂₀ C ₁₂ HgN ₄ O ₄	C ₂₄ H ₂₀ Br ₂ HgN ₄ O ₄	C ₂₄ H ₂₀ HgI ₂ N ₄ O ₄
Formula weight	699.93	788.85	882.83
Crystal system	Monoclinic	Monoclinic	Monoclinic
Space group	P2 ₁ /c	P2 ₁ /c	P2 ₁ /c
a, Å	18.4292(3)	18.2680(16)	18.052(3)
b, Å	13.6689(2)	13.9475(11)	14.386(3)
c, Å	9.8057	9.9861(8)	10.1560(18)
α, °	90	90	90
β, °	90.3635(9)	91.326(4)	91.810(7)
γ, °	90	90	90
V, Å ³	2470.09(7)	2543.7(4)	2636.3(8)
Z	4	4	4
D _{calc} , Mg/m ³	1.882	2.060	2.224
F(000)	1352	1496	1640

Table 6. Cont.

$\mu(\text{Mo K}\alpha)$, mm^{-1}	6.486	9.230	8.217
Range (2θ) for data collection, deg	$3.71 \leq 2\theta \leq 56.70$	$3.67 \leq 2\theta \leq 52.11$	$3.62 \leq 2\theta \leq 56.70$
Independent reflections	6145 [R(Int) = 0.0357]	4984 [R(Int) = 0.0512]	6571 [R(Int) = 0.0448]
Data/restraints/parameters	6145/0/324	4984/0/321	6571/0/316
quality-of-fit indicator ^c	1.048	1.044	1.034
Final R indices [I > 2 σ (I)] ^{a,b}	R1 = 0.0285, wR2 = 0.0689	R1 = 0.0535, wR2 = 0.1408	R1 = 0.0396, wR2 = 0.0929
R indices (all data)	R1 = 0.0366, wR2 = 0.0722	R1 = 0.0760, wR2 = 0.1506	R1 = 0.0592, wR2 = 0.1008

^a $R_1 = \sum ||F_o| - |F_c|| / \sum |F_o|$. ^b $wR_2 = [\sum w(F_o^2 - F_c^2)^2 / \sum w(F_o^2)^2]^{1/2}$. $w = 1/[\sigma^2(F_o^2) + (ap)^2 + (bp)]$, $p = [\max(F_o^2 \text{ or } 0) + 2(F_c^2)]/3$. $a = 0.0141$, $b = 0.4522$ for **1**; $a = 0.0348$, $b = 1.304$ for **2**; $a = 0.0127$, $b = 3.7802$ for **3**; $a = 0.0453$, $b = 2.4854$ for **4**; $a = 0.0341$, $b = 5.0712$ for **5**; $a = 0.0296$, $b = 13.8466$ for **6**; $a = 0.0331$, $b = 2.1145$ for **7**; $a = 0.0712$, $b = 13.7591$ for **8**; $a = 0.0468$, $b = 4.1899$ for **9**; ^c quality-of-fit = $[\sum w(|F_o^2| - |F_c^2|)^2] / (N_{\text{observed}} - N_{\text{parameters}})^{1/2}$.

4. Conclusions

Nine Hg(II) halide complexes containing bpba ligands with bulky and angular spacers were successfully synthesized. Complexes **1–3** containing the rigid **L**¹ ligands with bulky backbones showed bizarre supramolecular structures that were dependent on the identity of the halide anions, whereas the structural types of **4–6** containing the flexible **L**² ligands with bulky spacer and **7–9** constructed from the angular **L**³ ligands showed minimal dependence on the halide anions. The structural diversity of the bpba-based Hg(II) halide complexes and the effect of the halide anion are thus subject to the identities of the bpba ligands. Moreover, the bulkiness and the flexibility of the bpba ligands may also determine the effect of the halide anion. To further investigate the effect of halide anion on the structural diversity of flexible bpba-based Hg(II) complexes, future works can be geared towards the preparation of bpba ligands with more methylene groups [-(CH₂)_n-] in the backbone that can link the amide groups. Furthermore, reactions of mercury halide salts with flexible bpba ligands with C3 and C4 symmetries may also be investigated to afford Hg(II) complexes with interesting structural topologies. The sensing properties of **7–8** provide a unique insight into understanding the role of the halide anion in determining the quenching effect of the Hg(II) CPs by the metal ions, and the Hg-X---Fe³⁺ (X = Cl and Br) interactions may govern the quenching efficiency. Although toxic, Hg(II) halide complexes provide opportunities for the investigation of metal sensing.

Supplementary Materials: The following supporting information can be downloaded at: <https://www.mdpi.com/article/10.3390/ijms23147861/s1>.

Author Contributions: Investigation, M.G. and W.-C.H.; data curation, C.-Y.L., V.L., Y.-H.L. and P.B.S.; review and supervision, C.-H.L. and J.-D.C. All authors have read and agreed to the published version of the manuscript.

Funding: This research was funded by the Ministry of Science and Technology, Taiwan: MOST 109-2113-M-033-009.

Institutional Review Board Statement: Not applicable.

Informed Consent Statement: Not applicable.

Data Availability Statement: Data are contained within the article or Supplementary Materials.

Acknowledgments: We are grateful to the Ministry of Science and Technology of the Republic of China for support.

Conflicts of Interest: The authors declare no conflict of interest.

References

1. Lustig, W.P.; Mukherjee, S.; Rudd, N.D.; Desai, A.V.; Li, J.; Ghosh, S.K. Metal-organic frameworks: Functional luminescent and photonic materials for sensing applications. *Chem. Soc. Rev.* **2017**, *46*, 3242–3285. [[CrossRef](#)] [[PubMed](#)]
2. Li, B.; Wen, H.-M.; Cui, Y.; Zhou, W.; Qian, G.; Chen, B. Emerging Multifunctional Metal-Organic Framework Materials. *Adv. Mater.* **2016**, *28*, 8819–8860. [[CrossRef](#)] [[PubMed](#)]
3. Wales, D.J.; Grand, J.; Ting, V.P.; Burke, R.D.; Edler, K.J.; Bowen, C.R.; Mintova, S.; Burrows, A.D. Gas sensing using porous materials for automotive applications. *Chem. Soc. Rev.* **2015**, *44*, 4290–4321. [[CrossRef](#)] [[PubMed](#)]
4. Morsali, A.; Masoomi, M.Y. Structures and properties of mercury(II) coordination polymers. *Coord. Chem. Rev.* **2009**, *253*, 1882–1905. [[CrossRef](#)]
5. Mahmoudi, G.; Zareba, J.K.; Bauzá, A.; Kubicki, M.; Bartyzel, A.; Keramidis, A.D.; Butusov, L.; Mirosławh, B.; Frontera, A. Recurrent supramolecular motifs in discrete complexes and coordination polymers based on mercury halides: Prevalence of chelate ring stacking and substituent effects. *CrystEngComm* **2018**, *20*, 1065–1076. [[CrossRef](#)]
6. Rana, L.K.; Sharma, S.; Hundal, G. First report on crystal engineering of Hg(II) halides with fully substituted 3,4-pyridinedi carboxamides: Generation of two-dimensional coordination polymers and linear zig-zag chains of mercury metal ions. *Cryst. Growth Des.* **2016**, *16*, 92–107. [[CrossRef](#)]
7. Mahmoudi, G.; Bauzá, A.; Gurbanov, A.V.; Zubkov, F.I.; Maniukiewicz, W.; Rodriguez-Diéguez, A.; López-Torres, E.; Frontera, A. The role of unconventional stacking interactions in the supramolecular assemblies of Hg(II) coordination compounds. *CrystEngComm* **2016**, *18*, 9056–9066. [[CrossRef](#)]
8. Mobin, S.M.; Srivastava, A.K.; Mathur, P.; Lahiri, G.K. Reversible single-crystal to single-crystal transformations in a Hg(II) derivative. 1D-polymeric chain \rightleftharpoons 2D-networking as a function of temperature. *Dalton Trans.* **2010**, *39*, 8698–8705. [[CrossRef](#)]
9. Mahmoudi, G.; Khandar, A.A.; White, J.; Mitoraj, M.P.; Jena, H.S.; Der Voort, P.V.; Qureshi, N.; Kirillov, A.M.; Robeyns, K.; Safin, D.A. Polar protic solvent-trapping polymorphism of the HgII-hydrazone coordination polymer: Experimental and theoretical findings. *CrystEngComm* **2017**, *19*, 3017–3025. [[CrossRef](#)]
10. Yuan, Z.Z.; Luo, F.; Song, Y.-M.; Sun, G.-M.; Tian, X.-Z.; Huang, H.-X.; Zhu, Y.; Feng, X.-F.; Luo, M.-B.; Liu, S.-J.; et al. Solvent-induced supramolecular isomers, structural diversity, and unprecedented in situ formation of both inorganic and organic ions in inorganic–organic mercury(ii) complexes. *Dalton Trans.* **2012**, *41*, 12670–12673. [[CrossRef](#)]
11. Wang, H.; Wang, P.; Huang, C.; Chang, L.; Wu, J.; Hou, H.; Fan, Y. Construction of a series of mercury(II) complexes based on a bis-pyridyl-bis-amide ligand: Effect of counter anions, interactions on the supermolecular structures. *Inorg. Chim. Acta* **2011**, *378*, 326–332. [[CrossRef](#)]
12. Hsu, W.; Li, Y.-S.; He, H.-Y.; Chen, K.-T.; Wu, H.-S.; Proserpio, D.M.; Chen, J.-D.; Wang, J.-C. Stepwise formation of heteronuclear coordination networks based on quadruple-bonded dimolybdenum units containing formamidinate ligands. *CrystEngComm* **2014**, *16*, 7385–7388. [[CrossRef](#)]
13. Hsu, W.; Yang, X.-K.; Chhetri, P.M.; Chen, J.-D. Hg(II) coordination polymers based on *N,N'*-bis(pyridine-4-yl)formamidine. *Polymers* **2016**, *8*, 137. [[CrossRef](#)] [[PubMed](#)]
14. Mahat Chhetri, P.; Yang, X.-K.; Chen, J.-D. Solvent-mediated reversible structural transformation of mercury iodide coordination polymers: Role of halide anions. *Cryst. Growth Des.* **2017**, *17*, 4801–4809. [[CrossRef](#)]
15. Mahat Chhetri, P.; Yang, X.-K.; Chen, J.-D. Mercury halide coordination polymers exhibiting reversible structural transformation. *CrystEngComm* **2018**, *20*, 2126–2134. [[CrossRef](#)]
16. Mahat Chhetri, P.; Yang, X.-K.; Yang, C.-Y.; Chen, J.-D. One-dimensional Mercury Halide Coordination Polymers Based on a Semi-rigid N-donor Ligand: Reversible Structural Transformation. *Polymers* **2019**, *11*, 436. [[CrossRef](#)]
17. Mahat Chhetri, P.; Yang, X.-K.; Chen, J.-D. Isostructural Hg(II) halide coordination polymers: A comparison of powder XRD, IR, emission and Hirshfeld Surface Analysis. *J. Mol. Struct.* **2021**, *1239*, 130543. [[CrossRef](#)]
18. Thapa, K.B.; Hsu, Y.-F.; Lin, H.-C.; Chen, J.-D. Hg(II) supramolecular isomers: Structural transformation and photoluminescence change. *CrystEngComm* **2015**, *17*, 7574–7582. [[CrossRef](#)]
19. Kreno, L.E.; Leong, K.; Farha, O.K.; Allendorf, M.; Van Duyne, R.P.; Hupp, J.T. Metal–organic framework materials as chemical sensors. *Chem. Rev.* **2012**, *112*, 1105–1125. [[CrossRef](#)]
20. Allendorf, M.D.; Bauer, C.A.; Bhakta, R.K.; Houk, R.J.T. Luminescent metal-organic frameworks. *Chem. Soc. Rev.* **2009**, *38*, 1330–1352. [[CrossRef](#)]
21. Mac, M.; Danel, A.; Kizior, K.; Nowak, P.; Karocki, A.; Tokarczyk, B. Investigations of the heavy atom effect occurring in bianthryl and 10,10'-dibromobianthryl. Fluorescence, cyclovoltamperometric and actinometric studies. *Phys. Chem. Chem. Phys.* **2003**, *5*, 988–997. [[CrossRef](#)]
22. Ge, F.-Y.; Sun, G.-H.; Meng, L.; Ren, S.-S.; Zheng, H.-G. Four New Luminescent Metal–Organic Frameworks as Multifunctional Sensors for Detecting Fe³⁺, Cr₂O₇²⁻ and Nitromethane. *Cryst. Growth Des.* **2020**, *20*, 1898–1904. [[CrossRef](#)]
23. Zhang, S.-H.; Zhang, S.-Y.; Li, J.-R.; Huang, Z.-Q.; Yang, J.; Yue, K.-F.; Wang, Y.-Y. Rational synthesis of an ultra-stable Zn(ii) coordination polymer based on a new tripodal pyrazole ligand for the highly sensitive and selective detection of Fe³⁺ and Cr₂O₇²⁻ in aqueous media. *Dalton Trans.* **2020**, *49*, 11201–11208. [[CrossRef](#)] [[PubMed](#)]
24. Tripathi, S.; Bardhan, D.; Chand, D.K. Multistimuli-Responsive Hydrolytically Stable “Smart” Mercury(II) Coordination Polymer. *Inorg. Chem.* **2018**, *57*, 11369–11381. [[CrossRef](#)]

25. Pamei, M.; Puzari, A. Luminescent transition metal–organic frameworks: An emerging sensor for detecting biologically essential metal ions. *Nano-Struct. Nano-Objects* **2019**, *19*, 100364. [[CrossRef](#)]
26. Yang, X.-K.; Lee, W.-T.; Hu, J.-H.; Chen, J.-D. Zn(II) and Cd(II) coordination polymers with a new angular bis-pyridyl-bis-amide: Synthesis, structures and sensing properties. *CrystEngComm* **2021**, *23*, 4486–4493. [[CrossRef](#)]
27. Yu, Z.-Q.; Pan, M.; Jiang, J.-J.; Liu, Z.-M.; Su, C.-Y. Anion Modulated Structural Diversification in the Assembly of Cd(II) Complexes Based on a Balance-like Dipodal Ligand. *Cryst. Growth Des.* **2012**, *12*, 2389–2396. [[CrossRef](#)]
28. Ganguly, S.; Parveen, R.; Dastidar, P. Rheoreversible Metallogels Derived from Coordination Polymers. *Chem. Asian J.* **2018**, *13*, 1474–1484. [[CrossRef](#)]
29. Kumar, G.; Turnbull, M.M.; Thakur, V.; Gupta, S.; Trivedi, M.; Kumar, R.; Husain, A. Solvothermal synthesis, structural characterization, DFT and magnetic studies of a dinuclear paddlewheel Cu(II)-metallamacrocycle. *J. Mol. Struct.* **2020**, *1201*, 127193. [[CrossRef](#)]
30. Bruker AXS. APEX2, V2008.6, SADABS V2008/1, SAINT V7.60A, SHELXTL V6.14; Bruker AXS Inc.: Madison, WI, USA, 2008.
31. Sheldrick, G.M. A short history of SHELX. *Acta Crystallogr.* **2008**, *A64*, 112–122. [[CrossRef](#)]